

Modal Analysis of CX-100 Rotor Blade and Micon 65/13 Wind Turbine

J. R. White¹, D. E. Adams², and M. A. Rumsey¹

¹Wind and Water Power Technologies, Sandia National Laboratories, Albuquerque, New Mexico 87123

²Department of Mechanical Engineering, Purdue University, West Lafayette, IN 47907-2031

NOMENCLATURE

HP	=	High pressure side of the rotor blade, predominantly upwind during operation
LP	=	Low pressure side of the rotor blade, predominantly downwind during operation
Flap-wise	=	Direction of rotor blade oriented from high-pressure to low-pressure side of the airfoil
Lead-lag	=	Direction of rotor blade oriented from lead-edge to trailing-edge along the chord of the airfoil
Span	=	Direction of rotor blade oriented from root to tip along the length of the rotor blade
SNL	=	Sandia National Laboratories Wind and Water Power Technologies Department

ABSTRACT

At the end of 2008 the United States became the largest producer of wind energy with 25,369 MW of electricity. This accounts for 1.25% of all U.S. electricity generated and enough to power 7 million homes. As wind energy becomes a key player in power generation and in the economy, so does the performance and reliability of wind turbines. To improve both performance and reliability, smart rotor blades are being developed that collocate reference measurements, aerodynamic actuation, and control on the rotor blade. Towards the development of a smart blade, SNL has fabricated a sensed rotor blade with embedded distributed accelerometer measurements to be used with operational loading methods to estimate the rotor blade deflection and dynamic excitation. These estimates would serve as observers for future smart rotor blade control systems. An accurate model of the rotor blade was needed for the development of the operational monitoring methods. An experimental modal analysis of the SNL sensed rotor blade (a modified CX-100 rotor blade) with embedded DC accelerometers was performed when hung with free boundary conditions and when mounted to a Micon 65/13 wind turbine. The modal analysis results and results from a static pull test were used to update an existing distributed parameter CX-100 rotor analytical blade model. This model was updated using percentage error estimates from cost functions of the weighted residuals. The model distributed stiffness parameters were simultaneously updated using the static and dynamic experimental results. The model updating methods decreased all of the chosen error metrics and will be used in future work to update the edge-wise model of the rotor blade and the full turbine model.

1 INTRODUCTION

The following work was performed to develop the approaches for producing an experimentally updated wind turbine model for the development of operational monitoring methods. The following work was focused on developing the model updating approach for the flap-wise stiffness of the CX-100 rotor blade.

1.1 Background & Motivation

Wind energy accounts for a significant portion of U.S. power generation capacity, currently 1.25%, and is predicted to grow to 20% by 2030 [1]. Consequently, wind turbine performance and reliability will become increasingly important. Estimates of wind forces applied to a wind turbine and the corresponding reaction forces/moments in the rotor blades, drivetrain bearings, and gearbox while in operation will be needed to identify and resolve damage and failure modes in the wind turbine. There are many general approaches to wind force estimation, such as: wind speed and direction measurements with inference models to estimate aerodynamic loads, aerodynamic sensors located on the rotor blade for direct estimation of aerodynamic loads, structural based sensor systems for loading estimation through structural models, and loading inference with typical wind turbine sensors (drivetrain rpm, generator torque, nacelle inertial measurement unit, etc.) used with turbine global state-space models for force estimation. In the following work a structural model is developed for an accelerometer based structural monitoring system for operational wind turbine rotor blades. The structural model will be used in future work to validate the expected sensor signals and then to evaluate the corresponding feature extraction methods (deflection and loading estimates). This system is envisioned to provide wind turbine operators and designers direct information on the dynamic and quasi-static rotor deflection and loading for monitoring of turbine performance, fatigue, and to facilitate potential design improvements. Additionally, the sensor system could serve as an operational observer in future advanced smart rotor blades that will actively adapt based on the wind force being applied to mitigate damaging loads.

1.2 Previous Work

Relevant prior works are those which acquire wind turbine modal data, those which use the modal data to validate a model, and those which improve on modal testing of wind turbines. Molenaar [2] performed an experimental modal analysis of a wind turbine with accelerometers distributed over the rotor blades and tower. The natural frequencies of the test were used for comparison with a state-space model of the same turbine. In addition, the damping from the experimental results was used to compare the transient response of the modeled wind turbine and actual wind turbine to a step input. The natural frequencies were used to validate the model parameters of the wind turbine; however, active updating of the model parameters was not discussed and the mode shapes were not used for any of the validation. Griffith et al. [3,4] presented results on updating a BSDS wind turbine rotor blade model using modal parameters and static deflection data with weighted residual cost functions. Furthermore, Griffith [5] continued that work by mounting the rotor blade in a vertical span-wise direction and mounting it to a known boundary mass on airbags to validate the accuracy of the model. The approach was used to validate the model using static and modal features and then estimate the effect of adding a well defined mass and spring onto the root. The hypothesis was that the model would be validated if the predicted change caused by the mass addition was the same as the actual change. Lastly, Griffith et al. [6] discussed the influence of a boundary condition that is, assumed to be free with soft elastic support straps, and the effects of mass loading from sensors on the natural frequencies and damping ratios. These works were used when planning the free and mounted modal testing that is presented in the following sections.

The model validated in this paper will be used for developing operational monitoring approaches. White et al. [7,8] discussed accelerometer based methods for the estimation of static and dynamic deflections and loads. The methods extract operational information from the quasi-static and dynamic accelerations. The coordinate transformations from the ground reference to a sensor mounted to the rotating blade were also defined.

1.3 Sensored Rotor Blade

SNL has fabricated a sensored rotor blade to investigate load monitoring and damage detection capabilities of accelerometers and Fiber Bragg sensors. The instrumented rotor blade is a 9 m CX-100 design with integrated carbon composite along the shear web. The rotor blade was fabricated by TPI Composites, RI with one array of fiber optic sensors installed during layup and a second fiber optic array and an accelerometer array surface mounted on the interior surface. The surface mount sensors were installed prior to joining the HP and LP sides of the rotor blade. The surface mounted sensor arrays were fully functional after blade manufacture and shipment to the USDA Conservation and Production Research Laboratory in Bushland, TX. The Fiber Bragg sensor array that was installed during layup suffered micro-bending failure of the fiber optic cable that limited the number of functioning sensors. The accelerometer array also suffered sensor failures once the rotor blade was mounted on

the wind turbine. Although the failure mode has not been fully defined, it is believed that electric static discharge from the wind passing over the blades produced a charge buildup on the rotor blade that was dissipated by discharging through the sensors, causing the sensor failures. Future work will be focused on mitigating the susceptibility of accelerometers to ESD.

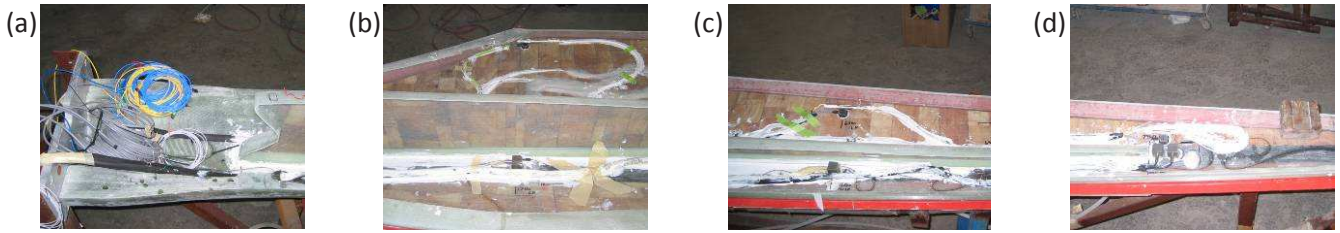


Figure 1: Sensorized rotor blade during fabrication with accelerometer arrays embedded on the high-pressure sides at span-wise distances of: (a) 0 m, (b) 1.74 m, (c) 6.5 m, and (d) 8 m.

2 EXPERIMENTAL TESTING

Experimental modal tests of the full wind turbine and rotor blade subcomponent were needed to validate a wind turbine model. In the following sections, a modal test of the CX-100 sensorized rotor blade was performed. The blade was hung by lifting straps with elastic bungee cord to replicate a free boundary condition. This setup was useful in validating the stiffness and mass properties of the blade with minimal influence by the boundary conditions. A modal test of the full wind turbine was also performed to account for the turbine tower and drivetrain effects on the rotor dynamics. The analysis showed that the rotor plane modes dominate the dynamics of the wind turbine through coupling of the hub and drivetrain.

2.1 Free-free Modal Testing

A modal test of the sensorized rotor blade was performed to estimate the natural frequencies, damping ratios, and mode shapes of the rotor blade. To estimate these characteristics independent of mounting conditions, the rotor blade was hung by elastic cables with the rotor blade oriented such that the desired excitation and response directions were perpendicular to gravity, as shown in [Figure 2](#) and [Figure 3a](#). By aligning gravity perpendicular to the direction of excitation, the effect of the elastic boundary condition was minimized as was the influence of the internal body forces produced by weight loading in the flap-wise direction.



Figure 2: Experimental setup for modal test of sensorized rotor blade with free boundary conditions.

In addition to the seven triaxial and three uniaxial accelerometers embedded in the rotor blade, eight ICP® triaxial sensors (PCB 356A14 and 356A65) were temporarily mounted to the exterior surface, as shown in [Figure 3b](#). The sensor additions provided additional reference for modal parameter estimation. The rotor blade was excited by a modal impact hammer (PCB 086C03) with a soft rubber impact tip for low frequency excitation and a rear mounted mass for increased impact energy transfer as shown in [Figure 3c](#). A VXI Technologies data acquisition system was used to measure the excitation and response signals. X-Modal2© software from the University of Cincinnati Structural Dynamics Research Laboratory was used to curve fit the frequency response data and estimate natural frequencies, damping ratios, and mode shapes. The results of the test are shown in [Table 1](#).

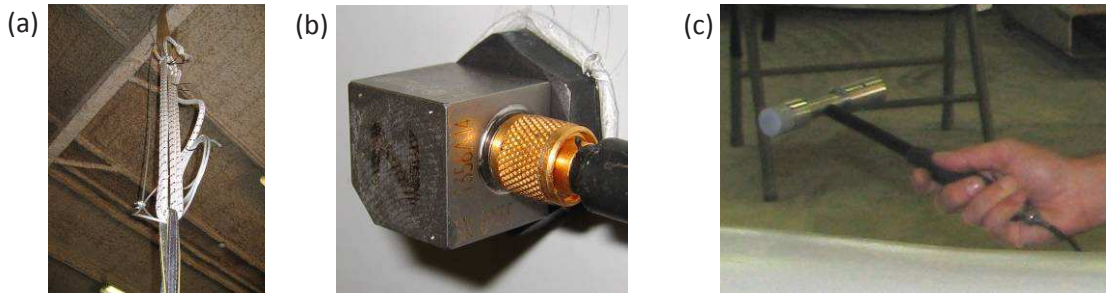


Figure 3: (a) Elastic support strap for test. (b) Externally mounted supplemental triaxial accelerometer. (c) Modal impact hammer with soft compliant tip and additional hammer mass.

The first mode of vibration of the rotor blade was a flap-wise bending mode, which was similar to the first beam-bending mode shape, at 8.2 Hz. The modal results showed that flap-wise and lead-lag bending mode shapes accounted for the first six modal features of the rotor blade. The seventh mode was a torsional oscillation about the span-wise direction. The flap-wise modes occurred at lower frequencies than the lead-lag modes because the second moment of area was smaller about the lead-lag axis than about the flap-wise axis for all airfoil cross sections (cross-sections outboard of 10% span-wise length). The damping of the first mode was also smaller than the other modes, which meant that the first flap bending mode was likely to respond for the longest period of time after excited.

As mentioned previously, the rotor blade was tested with the flap-wise direction perpendicular to gravity and the lead-lag direction parallel to gravity. This orientation could have led to errors in the lead-lag direction as support straps were directly actuated when the rotor blade was excited in the lead-lag direction. The rigid body mode shape in the lead-lag direction was at a frequency less than one-tenth of the first lead-lag flexible mode of 16.8 Hz. A general rule of thumb for free boundary conditions is that they separate the rigid and flexible body modes by a factor of at least ten. This characteristic of free supports is used to minimize the influence of the boundary condition on the natural frequencies. Additionally, the support straps were located at the nodes of the first flap-wise bending mode to further minimize the influence of the boundary conditions. By hanging the rotor blade vertically with the tip down, the most ideal orientation for modal testing is realized because the flap and lead-lag directions are perpendicular to gravity in this orientation thereby minimizing gravitational and boundary effects.

Table 1: Modal results for CX-100 rotor blade with free boundary conditions.

Mode	Frequency (Hz)	Damping (% critical)	Description
1	8.2	0.28	1st Flap Bending
2	16.8	0.62	1st Lag Bending
3	20.3	0.49	2nd Flap Bending
4	33.8	0.51	3rd Flap Bending
5	42.2	1.17	2nd Lag Bending
6	52.2	0.58	4th Flap Bending
7	60.6	1.16	1st Torsion
8	69.9	0.74	3rd Lag Bending

The estimated natural frequencies and mode shapes were assumed to be sufficiently accurate to update the distributed parameter model available for the CX-100 rotor blade. However, in order to investigate the full wind turbine distributed parameter model generated by FAST in MSC.ADAMS, a full wind turbine modal analysis was performed with the sensed rotor blade and two unsensed rotor blades mounted to the wind turbine.

2.2 Full Turbine Testing

A modal test of the sensed rotor blade mounted to the Micon 65/13 wind turbine located in Bushland, TX was performed. Figure 4a shows the sensed rotor blade mounted to the wind turbine and oriented vertically downward. Two unsensed CX-100 rotor blades were also mounted to the wind turbine for the modal and operational testing. In addition to the sensors embedded in the sensed blade, a triaxial accelerometer was temporarily mounted to the tip of each rotor blade, four biaxial sensors were mounted to the drivetrain, the inertial

measurement unit mounted in the nacelle was also used as a reference accelerometer, and two triaxial sensors were mounted across the mounting flange of the sensed rotor blade for a total of forty-seven simultaneously sampled acceleration measurements. Thirty-four locations on the sensed rotor blade, fourteen locations on each of the unsensed rotor blades, four locations on the drivetrain, and sixteen locations on the tower for a total of eighty-two locations were excited with an impact hammer to estimate the modal parameters. Five averages were acquired at each impact location and the data was recorded with a VXI Technologies HPE 1432a data acquisition system.



Figure 4: (a) Micon 65/13 Wind Turbine with the Sensed Rotor Blade mounted. (b) Modal impact testing of the wind turbine rotor blades. (c) Modal impact testing of the wind turbine tower.

Data acquired during the modal test was used to estimate frequency response functions, which were imported into X-Modal2© along with the spatial location of each impact and reference sensor location and orientation. An example of the mode shapes produced, the first umbrella mode at 4.5 Hz, is shown in Figure 5. Modal analysis results showed that the tower of the turbine was very stiff and generally behaved as a rigid boundary condition, excluding the first two tower modes. Due to the rigid tower, the excitation and reference data from measurement degrees of freedom located on the rotor plane were selected as the input data for the experimental modal analysis.



Figure 5: 1st Umbrella Mode Shape of rotor plane from modal test experiment.

The results of the modal analysis are shown in Table 2. The table indicates that the first two modes were side-to-side and fore-aft tower modes, which were dominated by the stiffness of the tower and foundation and the mass of the tower and nacelle. Beyond the first two modes, the tower did not play a significant role in the motion of any other modes. The coupled system of the three rotor blades attached to the hub and connected to the low speed shaft dominated the modal features. Individual rotor blade modes were not evident, but instead the system of

rotor blades produced the modal frequencies and shapes. Experimental results showed that the stiffness of either the hub or low speed shaft was small enough to allow coupling of the rotor blades. If the hub and low speed shaft were truly rigid, with an infinitely large stiffness, then each blade would have had individual uncoupled modes. These modes would likely be very close to the same natural frequency and would be very similar to the frequencies and shapes observed in a cantilevered rotor blade modal test.

Table 2: Modal results for CX-100 rotor blades mounted to Micon 65/13 wind turbine.

Mode	Frequency (Hz)	Damping with Window (% critical)	Damping without Window (% critical)	Description
1	3.19	2.90	1.96	Side-Side Tower Mode
2	3.40	3.21	2.33	For-Aft Tower Mode
3	4.51	2.12	1.46	1st Umbrella Mode
4	5.51	1.05	0.51	1st Spoke Mode
5	6.36	3.30	2.84	1st Vertical Antisymmetric
6	7.16	1.66	1.25	1st Horizontal Antisymmetric
7	9.96	2.50	2.20	2nd Horizontal Antisymmetric
8	10.30	2.08	1.79	2nd Vertical Antisymmetric
9	11.49	1.05	0.79	2nd Umbrella Mode
10	15.41	1.31	1.12	1st Rotary Torsion

The results of this modal test provided sufficient information to extract the natural frequencies, damping ratios, and shapes for model verification and updating. In future work, excitation methods other than a modal impact hammer will be evaluated. An impact excitation produces a finite length time response. The length of the response time dictates the amount of low frequency information available in the estimated frequency response function. A higher energy impact would produce a higher signal to noise ratio time response; however, this type of impact would also require a lower sensitivity accelerometer for the initial spike in acceleration. The lower sensitivity accelerometer will increase the noise floor for both the modal testing and the operational monitoring that followed. In future work, alternate modal excitation methods will be attempted to improve the results.

3 MODEL UPDATE

The purpose of this section is to show how the CX-100 rotor blade distributed parameter model was simultaneously updated using static and dynamic local and global features. The emphasis of this section is a proposed approach using commonly installed sensors and typical “pre-flight” testing of a wind turbine rotor blade to update a computational model. Additionally, cost functions and error metrics are described that produce physically meaningful error percentages that can be compared to update model stiffness properties. Lastly, weighting functions are described to emphasize residuals when testing errors are less significant and de-emphasizing residuals when testing errors are more significant. Some of the weighting functions are also adjusted during model updating to expedite convergence.

3.1 Initial Model

A distributed parameter model of the CX-100 rotor blade including bending stiffness, mass, airfoil geometry, wall thickness, and span-wise section locations was available prior to model updating. The properties described could have been used for a lumped parameter model, such as a series of lumped masses connected by springs, or for a distributed parameter model, such as a series of Euler-Bernoulli beam elements with stiffness and mass properties. In this paper, a distributed parameter model was created using Euler-Bernoulli beam elements, which maintained smooth displacement at the nodes; that is, the displacement and slope at the nodes were continuous [8]. For example, the deflection of the rotor blade model caused by a 4.45 N (1 lbf, used for comparison with experimental data acquired in units of lbf) force at the 7.25 m span-wise location is shown in [Figure 6](#). This plot shows the slope and curvature along the rotor blade. It also illustrates the typical cantilevered beam bending shape for a discrete location force input, where there was zero deflection and slope at the root and constant slope and zero curvature at the tip. The curvature plot was discontinuous with each element showing a decrease in

curvature in the outboard span-wise direction. For an Euler-Bernoulli beam element with linear-elastic material properties, the curvature plot was related to the moment, stress, and strain through the following relationship:

$$EI \frac{\partial^2 u}{\partial z^2} = \frac{EI \varepsilon}{c} = \frac{I \sigma}{c} \quad (1)$$

where E was the modulus of elasticity, I was the second area moment, u was the displacement in the flap-wise direction, z was the span-wise location, ε was the elastic strain, c was the distance from the neutral bending axis, and σ was the elastic stress. In a simple form, the curvature and strain were related by:

$$\frac{\partial^2 u}{\partial z^2} = \frac{\varepsilon}{c}. \quad (2)$$

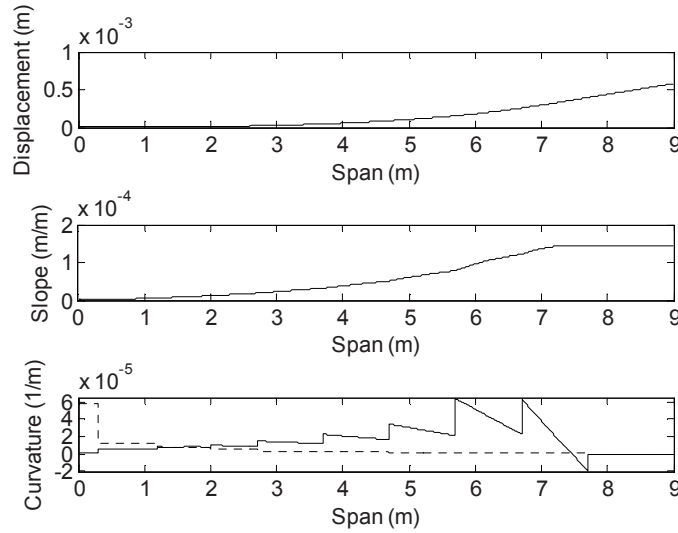


Figure 6: Displacement, slope, and curvature of distributed parameter finite element CX-100 rotor blade. The distribution of bending stiffness prior to model updating is shown in the curvature plot (dashed).

The moment from Equation (1) produced by a 4.45 N force applied to the rotor blade is linearly increased from a value of zero at a span-wise location of 7.25 m to a maximum value of 32 N-m at the rotor cantilevered connection as shown in Figure 7a. In this figure, the theoretical moment distribution along the rotor blade (dashed) was compared with the moment estimates from the HP and LP distributed strain gages that use the relationships in Equation (1). Experimental strain gage measurements were acquired during a static pull test at the 7.25 m span-wise location in the flap direction as shown in Figure 7b. Several deflection distances and force levels were tested to establish the strain-force (1/lbf) calibration of the rotor blade with strain gages. The slope of this calibration was the measured strain for a 1 lbf (4.45 N) applied force. The sensor estimates of moment from this data depended on the accuracy of the model bending stiffness, EI , and of the distance from the neutral axis, c . Strain gages located symmetrically across the neutral axis separated by a total distance h were used to improve the accuracy of the neutral axis distance through the relationship:

$$h = c_1 - c_2$$

$$c_1 = \frac{\varepsilon_1 h}{\varepsilon_1 - \varepsilon_2} \quad (3)$$

assuming that the line connecting the strain gages was perpendicular to the neutral axis and parallel to the cross sectional plane. The moment estimates from the strain gages also assumed that a distributed parameter Euler-Bernoulli approach was valid, which meant that during deflection the cross-sectional planes rotated an amount

equal to the slope of the deflection. Future work may evaluate whether this approximation was valid in wind turbine rotor blades, but for the scope of this work the model was assumed to be valid.

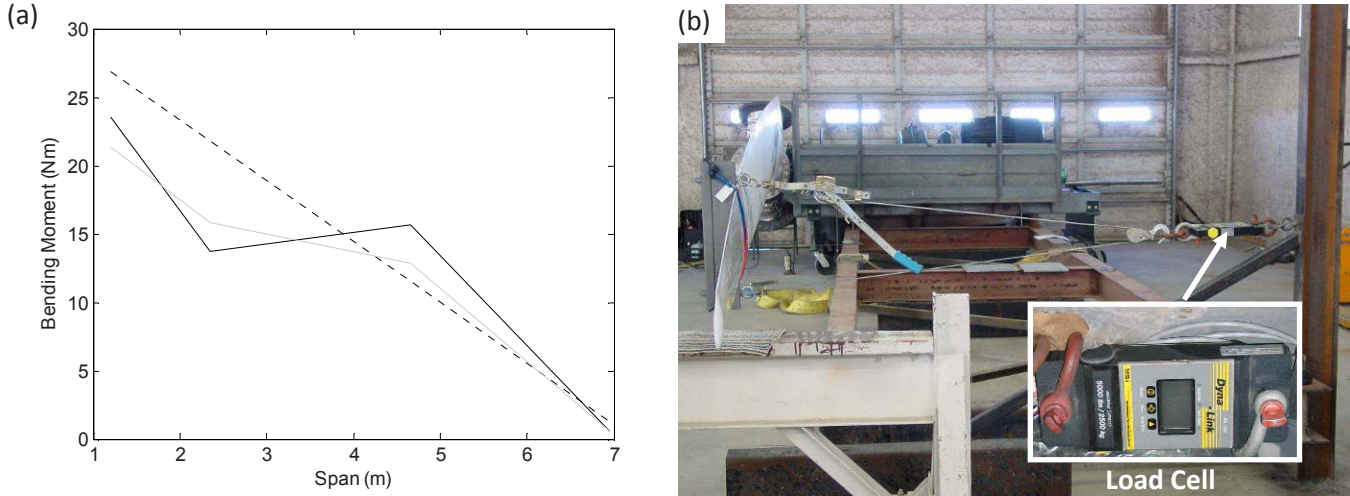


Figure 7: (a) Bending moment prior to model updating with: finite element model (dashed), experimental results from high pressure side strain gages (black), and experimental results from low pressure side strain gages (gray). (b) Static flap-wise pull fixture with in-line load cell.

The initial distributed parameter model stiffness and mass matrices were also used to estimate the free boundary condition modal frequencies and shapes. The natural frequency results prior to model updating are listed in [Table 3](#) and the shapes are shown in [Figure 10](#). The results showed a significant difference between the experimental and model modal frequencies and shapes prior to model updating.

3.2 Model Updating

The previous sections showed the discrepancies between the experimental and analytically modeled static pull and modal analysis results. Having quantified the differences, the next step was to determine quantifiable error indicators from several sources of experimental and analytical errors that could be equally compared to determine how to best update the distributed property parameters. The following work was mostly focused on updating the eleven distributed bending stiffness properties. The distributed mass property could be directly measured from section cuts of the rotor blade when the testing was completed. However, the distributed mass applied to each element length and then summed was 20% lower than the actual measured mass. To account for this deviation, each distributed mass property was increased by 25%.

To update the stiffness properties, a percentage error metric was created from the difference in critical features of the experimental and model results. For each of the static and modal results, one feature dominated by the overall stiffness and one feature dominated by the local stiffness was estimated, for a total of four types of features. The balance of local and global stiffness updates was assumed to improve the model updating by minimizing the constraints on the individual stiffness parameter changes.

The cost function J was used to calculate the weighted square of the residuals:

$$J = e^T W e \quad (4)$$

where e was the residual and W was the weighting function. An example of a residual that was used is the comparison of the experimental and model mode shapes:

$$e = \begin{Bmatrix} U_{\text{model } 1,r} - U_{\text{experiment } 1,r} \\ \vdots \\ U_{\text{model } p,r} - U_{\text{experiment } p,r} \end{Bmatrix} \quad (5)$$

for a mode r where U was the mode shape displacement coefficient at a location p . The weighting function was a diagonal matrix with each diagonal term corresponding to the weighting of an individual residual:

$$W = \text{diag}\{w_1 \quad \cdots \quad w_p\}. \quad (6)$$

For equally weighted residuals, this matrix was the identity matrix. For the case of the mode shapes, the weighting was based on the mode shape itself because locations with small modal deflection corresponded to node locations that were sensitive to small errors in testing location accuracy, whereas locations with large modal deflection corresponded to anti-node locations and were not nearly as sensitive to testing inaccuracy. Weighting by the modal deflection therefore emphasized the model updating on the residuals that were most likely attributed to model errors and de-emphasized the residuals that corresponded to possible testing limitations, i.e. issues with the dynamic range of experimental data. To produce weighting that did not bias residuals in comparison to other modes and other error metrics, the absolute value of the mode shape displacement coefficient for a mode r was divided by the sum of the absolute value of all displacement coefficients for that mode shape:

$$W = \text{diag}\left\{ \frac{|U_{\text{model } 1,r}| \cdot n}{\sum_{i=1}^n |U_{\text{model } i,r}|} \quad \cdots \quad \frac{|U_{\text{model } n,r}| \cdot n}{\sum_{i=1}^n |U_{\text{model } i,r}|} \right\} \quad (7)$$

and then multiplied by the total number of displacement coefficients of that mode, n . The division of each modal displacement coefficient by the total produced an absolute percentage of the total model displacement distributed at each location. If all n locations were weighted equally, then the total weight would be n . In this case the percentage distribution of n was established. For example a location of significant modal response had a weighting function greater than one, but a location with small modal response had a weighting function less than one. The total weighting however was the same as for an equally weighted case. The other advantage of this weighting approach was that the model mode shape, not the experimental shape, itself was used to establish the weighting function. In this case, the weighting function changed its distribution as the model was updated.

The cost function, J , that resulted from this process was the sum of the weighted square of the residuals for a given mode shape. To compare this residual with other error metrics, it was converted into an estimate of the percentage error of the modeled mode shape. To do this the square root of the cost function was divided by the absolute sum of the modal displacement coefficients for the experimental mode shape. The percentage error of all three mode shapes was compared with the percentage error between the experimental and model natural frequencies. As mentioned previously, local and global stiffness error metrics were used to minimize the constraints placed on the parameter updating. For the modal results, the mode shape was used as the local error metric as it was more sensitive to localized changes in the stiffness parameters and the natural frequencies were used as the global error metric as they were less sensitive to localized changes to the stiffness parameters.

A similar approach was used for the static moment comparison. For the global error metric a first order polynomial was fit through the theoretical and experimentally estimated moment distributions. The percentage difference between the slopes of the two polynomials, using the theoretical estimate as a reference, was used for comparison. For the local error metric, the cost function was calculated for the residuals between the individual moment estimates (HP and LP estimates at 1.2 m, 2.35 m, 4.65 m, and 6.95 m) and the theoretical moment at those span-wise locations and weighted by the normalized theoretical moment distribution. This weighting function emphasized measurements near the root area where the moment magnitude was a maximum and de-emphasized measurements near the applied force location where the moment magnitude was a minimum.

The preceding calculation produced local and global percentage error estimates, E , for the first three mode shapes and natural frequencies, for the slope of the moment distribution estimated from the strain gages, and for the individual moment estimates. The global error metric that was optimized was:

$$E_{total} = \sum E_{natural\ frequency} + \sum E_{mode\ shape} + 3\sum E_{moment\ slope} + 3\sum E_{moment\ residual} \quad (8)$$

where the static errors were weighted by a factor of three so that the static error was equally weighted with the total dynamic error produced from the summation of the error of the first three mode shapes. To minimize the total error, the **fminsearch** function in MATLAB® was used. This function implemented the Nelder-Mead simplex multiple degree of freedom nonlinear optimization method [10].

3.3 Updated Model

The simultaneous model update was performed on a standard desktop PC with dual-core 2.0 Ghz processor and 2 GB of RAM with a run time of approximately one minute. Figure 8a illustrates the original distribution of blade stiffness (dashed) and the updated distribution of stiffness (solid) on a logarithmic plot. This plot shows that the stiffness was increased outboard of the 4.5 m location and was decreased significantly in the first 1 m of the blade length. The moment estimated by the strain gages is shown in Figure 9, which showed closer agreement between the estimated moment and theoretical moment than for the original stiffness properties that were used in Figure 7a. The natural frequency estimates were also significantly closer to the experimental results after model updating as listed in Table 3. The updated mode shapes (solid) also showed closer agreement with the experimental mode shapes (circles) as shown in Figure 10.

The updated model showed closer agreement to all of the static and dynamic error metrics calculated. The significant decrease in the stiffness of the inboard region of the rotor blade was concerning as that much of a reduction in stiffness was not realistic. However in that region there were minimal measurements because all three mode shapes de-emphasized the weighting in that region and there were only two strain measurements located inboard of the 1 m station at 0.35 m. Additionally, the distributed mass was not updated, which could have affected the changes to this region where the mass distribution was most significant as shown by Figure 8b. In the future, constraints could be defined so that individual stiffness could not be changed without affecting the adjacent stiffnesses or additional sensor locations and measurements could be acquired specifically focused on the inboard spans of concern.

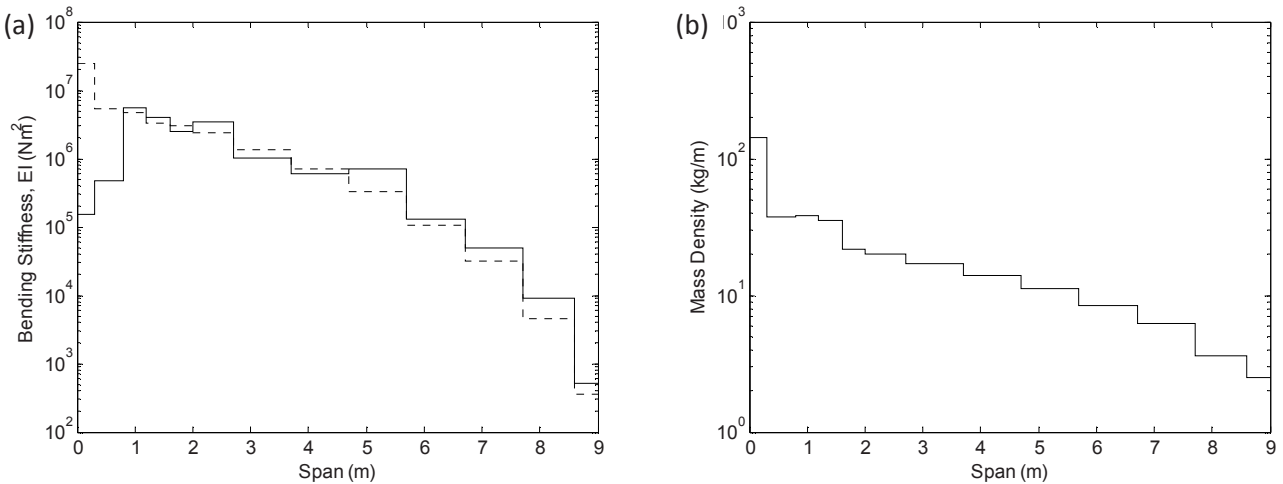


Figure 8: (a) Comparison of distributed bending stiffness properties before (dashed) and after (solid) model updating. (b) Distributed mass density (kg/m) of CX-100 rotor blade.

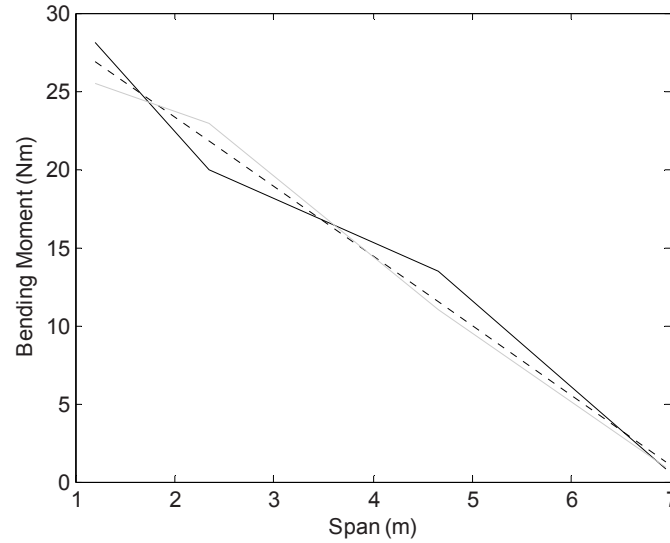


Figure 9: Bending moment after model updating with: finite element model (dashed), experimental results from high pressure side strain gages (black), and experimental results from low pressure side strain gages (gray).

Table 3: Comparison of experimental and finite element modal frequencies before and after model updating.

Mode	Experimental Frequency (Hz)	Model Frequency Prior to Updating		Model Frequency After Updating		Description
		Hz	% Difference	Hz	% Difference	
1	8.2	6.94	-16%	8.13	-1%	1st Flap Bending
2	20.3	15.90	-22%	18.28	-10%	2nd Flap Bending
3	33.8	29.53	-13%	33.84	0%	3rd Flap Bending

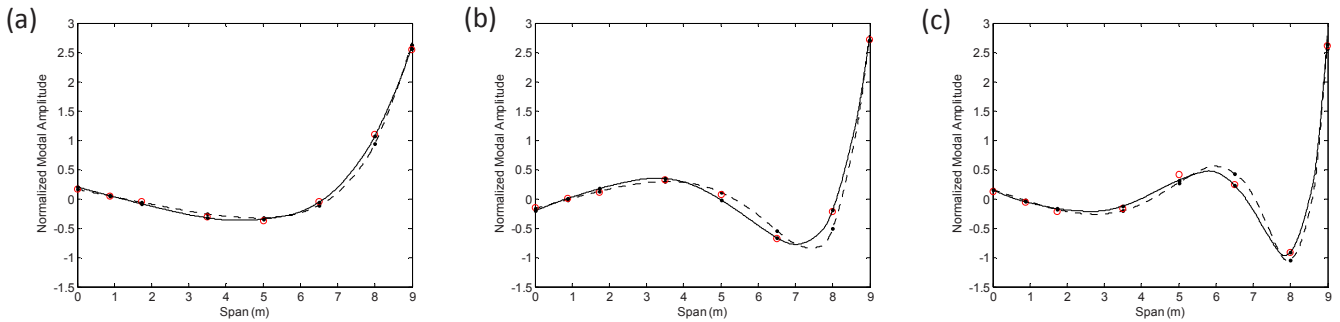


Figure 10: Comparison of the first three flap-wise bending modes at (a) 8.2 Hz, (b) 20.3 Hz, and (c) 33.8 Hz where the experimental mode shape coefficients are (point circle), mode shape before model updating is (dashed), and mode shape after model updating is (solid).

4 FUTURE WORK

The preceding work demonstrated the use of a combination of static and dynamic test data for the updating of a CX-100 rotor blade flap-wise stiffness properties. In future efforts, these approaches will be expanded to update the flap-wise and edge-wise stiffness and mass properties of the CX-100 rotor blade. Additionally, the full turbine experimental modal analysis results will be used in conjunction with a previous wind turbine tower modal analysis to update the stiffness and mass properties of the combined wind turbine system. The individually updated rotor blade and tower models will be used to determine the degrees of freedom, stiffness, and mass properties of the connections that are needed to construct a full turbine model. [Table 4](#) lists the experimental natural frequencies

of the turbine modal analysis in comparison to the natural frequencies of the current CX-100 Micon 65/13 wind turbine model. Both the experimental and computational models contain the same modes, however the frequencies have significant errors that will require boundary condition / attachment model updating.

Table 4: Comparison of experimental and MSC.ADAMS frequencies for full turbine model.

Mode	Modal Test Frequency (Hz)	MSC.ADAMS Frequency (Hz)	Description
1	3.19	2.62	Side-Side Tower Mode
2	3.40	2.62	For-Aft Tower Mode
3	4.51	4.69	1st Umbrella Mode
4	5.51	7.28	1st Spoke Mode
5	6.36	4.58	1st Vertical Antisymmetric
6	7.16	4.62	1st Horizontal Antisymmetric
7	9.96	11.95	2nd Horizontal Antisymmetric
8	10.30	11.77	2nd Vertical Antisymmetric
9	11.49	12.08	2nd Umbrella Mode
10	15.41	7.19	1st Rotary Torsion

5 CONCLUSIONS

To aid in future operational monitoring system development, an experimentally updated wind turbine model was needed that accurately reflected the operational dynamics of the CX-100 Micon 65/13 wind turbine. Experiments were performed to acquire the modal frequencies, damping ratios, and mode shapes of the CX-100 sensed rotor blade in free boundary conditions and of the same rotor blade mounted to the wind turbine with two other unsensed rotor blades. Static pull tests were also performed to calibrate the strain-force relationships of the embedded strain gages. The experimental results were used to update the distributed stiffness properties using percentage errors generated from cost functions of weighted residuals. The results of the model update made improvements to all of the error metrics. Some of the changes to the distributed stiffness properties may not have been physically accurate and will need to be improved in future development of the methods. In future work, the methods presented will be expanded to include edge-wise motion of the rotor blade and a full turbine model including the wind turbine rotor plane, tower, and connections.

6 ACKNOWLEDGEMENTS

The results presented in this work were made possible by the US Department of Energy Sandia National Laboratories System Modeling Tools & Analysis Sensors Task performed by the Wind and Water Power Technologies Department. The experimental results were made possible with help from B. Neal and A. Holman of the US Department of Agriculture Conservation and Production Research Laboratory. The strain gage experimental data analysis was performed by J. Berg of Sandia National Laboratories.

REFERENCES

1. American Wind Energy Association. "American Wind Energy Association Annual Wind Industry Report Year Ending 2008." US Energy Information Administration. AWEA. 2009. <http://www.awea.org/publications/reports/AWEA-Annual-Wind-Report-2009.pdf> (accessed September, 2009)
2. Molenaar, D. P., "Experimental Modal Analysis of a 750 kW Wind Turbine for Structural Model Validation," 41st AIAA Aerospace Sciences Meeting and Exhibit, 2003, Reno, NV.
3. Griffith, D. T., Paquette, J. A., and Carne, T. G., "Development of Validated Blade Structural Models," 46th AIAA Aerospace Sciences Meeting and Exhibit, 2008, Reno, NV.

4. Griffith, D. T. and Carne, T.G, "Experimental Uncertainty Quantification of Modal Test Data," 25th International Modal Analysis Conference, February 2007, Orlando, FL, USA.
5. Griffith, D. T., "Structural Dynamics Analysis and Model Validation of Wind Turbine Structures," 50th AIAA/ASME/ASCE/AHS/ASC Structures, Structural Dynamics, and Materials Conference, 2009, Palm Springs, FL.
6. Griffith, D. T., Carne, T. G., and Paquette, J. A., "Modal Testing for Validation of Blade Models," Society for Experimental Mechanics Annual Conference, 2009, Albuquerque, NM.
7. White, J. R., Adams, D. E., and Rumsey, M. A., "Operational Load Estimation of a Smart Wind Turbine Rotor Blade," SPIE Smart Structures and Materials & Nondestructive Evaluation and Health Monitoring: Health Monitoring of Structural and Biological Systems, 2009, San Diego, CA.
8. White, J. R., Adams, D. E., and Rumsey, M. A., "Sensor Acceleration Potential Field Identification of Wind Turbine Rotor Blades," 7th International Workshop on Structural Health Monitoring, 2009, Stanford, CA.
9. Cook, R. D., Malkus, D. S., Plesha, M. E., and Witt, R. J., Concepts and Applications of Finite Element Analysis Fourth Edition, John Wiley & Sons, Inc., New York, NY.
10. Lagarias, J. C., Reeds, J. A., Wright, M. H., and Wright, P. E., "Convergence Properties of the Nelder-Mead Simplex Method in Low Dimension," SIAM Journal of Optimization, Vol. 9 Number 1, pp. 112-147, 1998.

Structural Dynamics and Renewable Energy, Volume 1
Proceedings of the 28th IMAC, A Conference on
Structural Dynamics, 2010
Proulx, T. (Ed.)
2011, X, 382 p., Hardcover
ISBN: 978-1-4419-9715-9